A Radiation Center Representation of Antenna Radiation Patterns on a Complex Platform

Caner Ozdemir, *Member, IEEE*, Rajan Bhalla, and Hao Ling, *Fellow, IEEE*

***Abstract*—A sparse model of the antenna radiation pattern on a complex platform is presented. This representation is based on a point radiator model that describes the radiation pattern by a collection of radiation centers on the platform. The methodology for obtaining the radiation center model is presented. It entails first generating the three-dimensional (3-D) antenna synthetic aperture radar (ASAR) imagery of the platform and then parameterizing the resulting image by a collection of point radiators via the CLEAN algorithm. It is shown that once such a representation is obtained, we can reconstruct and extrapolate antenna radiation patterns over frequencies and aspects with good fidelity, thus achieving high data compression ratio. Furthermore, it is shown that the resulting radiation center information can be used to pinpoint cause-and-effect in platform scattering and provide important guidelines for reducing platform effects.**

***Index Terms*—Antenna radiation patterns, scattering centers.**

I. Introduction

IT IS well known that the platform structure that supports an antenna can dramatically alter its radiation characteristics. Recently, we developed an imaging algorithm, termed antenna synthetic aperture radar (ASAR) imaging, to pinpoint the locations of secondary scattering off a mounting platform from the antenna radiation data [1]. Our approach is similar to the inverse synthetic aperture radar (ISAR) concept. Contrary to conventional ISAR imaging, a key complication of the ASAR imaging scenario is that the antenna is located in the near field of the platform. It was shown that under the small-angle approximation and single-bounce assumption, a Fourier transform relationship exists between multifrequency, multi-aspect radiation data and the three-dimensional (3-D) positions and strengths of the secondary scatterers on the platform. Therefore, a 3-D image showing the spatial locations of platform scattering can be constructed via Fourier inversion of the radiation data. This concept was demonstrated using the computed radiation data from the code Apatch [2], which employs the shooting and bouncing ray (SBR) technique [3]–[6]. Fig. 1 shows the CAD model of an airplane with a small vertical dipole antenna placed above the cockpit. The entire airplane is assumed to be perfectly conducting. By collecting the multiple frequency (10-GHz with 0.56-GHz bandwidth) and multiple aspect (3.33° azimuth window and 1.72° elevation window about the nose) radiation pattern, a 3-D image can be formed from the ASAR algorithm. Shown in Fig. 2(a) is the 3-D ASAR image viewed along various horizontal cuts through the airplane. The key scattering locations near the nose and wings of the airplane can be clearly identified. This is very similar to an ISAR image in which the strong scattering locations on the target are displayed to facilitate signature reduction and target identification applications.

In this paper, we extend the work in [1] by extracting a sparse representation of the ASAR imagery. This is motivated by the observation that similar to an ISAR image, ASAR images exhibit strong point-scatterer like behavior. Since it is well known that the backscattered signature can be modeled by a very sparse set of scattering centers on the target [6]–[9], we believe it is also possible to parameterize the radiation patterns of an antenna mounted on a complex platform via a set of "*radiation centers*." Using an approach similar to our recent work on scattering center extraction [6], we utilize the CLEAN algorithm [10], [11] to carry out the radiation center extraction process from an ASAR image. It is shown that once such a representation is obtained, we can reconstruct and extrapolate antenna radiation patterns over frequencies and angles with good fidelity, thus achieving high data compression ratio. Furthermore, it is shown that when coupled with the SBR simulation engine, the resulting radiation center information can be used to pinpoint cause-and-effect in platform scattering and provide important guidelines for reducing platform effects.

This paper is organized as follows. In Section II, we first review the ASAR image formation algorithm and present the radiation center model of the antenna radiation data. Next, we apply the CLEAN algorithm to carry out the extraction process and examine the sparseness of the model and the fidelity of the reconstructed data in frequency and aspect. In Section III, we demonstrate two utilities of the radiation center representation. In the first example, we show that the antenna radiation pattern can be extrapolated over aspect due to the angular stability of the radiation center model. Consequently, it is possible to represent the complex radiation pattern over all observable angles using the radiation centers extracted at only a limited number of angles. In the second example, we carry out a study to reduce platform effects. It is shown that the extracted radiation center information from the SBR simulation engine can be exploited to identify those parts of the target that give rise to significant secondary radiation. Consequently, by placing absorbers over a limited portions of the platform, it is possible to suppress a majority of the platform scattering.

Manuscript received September 30, 1997; March 8, 2000. This work was supported by the Air Force MURI Center for Computational Electromagnetics under Contract AFOSR F49620-96-1-0025 and in part by the Office of Naval Research under Contract N00014-98-1-0178.

C. Ozdemir is with the Department of Electrical and Electronics Engineering, Mersin University, 33342 Mersin, Turkey.

R. Bhalla is with SAIC-DEMACO, Boston, MA 01880 USA.

H. Ling is with the Department of Electrical and Computer Engineering, The University of Texas at Austin, Austin, TX 78712-1084 USA.

Publisher Item Identifier S 0018-926X(00)05785-9.

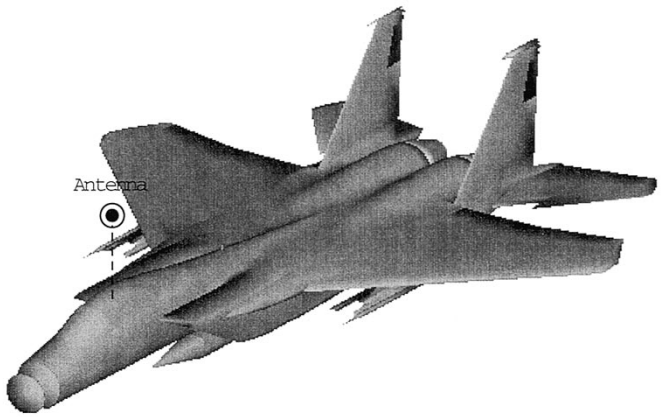

Fig. 1. CAD model of an airplane with a small vertical dipole antenna placed above the cockpit.

It should be noted that the numerical results used throughout this paper will be based on the SBR code Apatch, which does not include higher order scattering phenomena such as higher order diffractions and surface/creeping waves. Furthermore, the example configurations (e.g., dipole above aircraft) considered in this paper may not be construed as practical. However, we believe these limitations do not significantly detract from the main point of this paper, which is the concept of radiation center representation for modeling platform effects.

II. Radiation Center Extraction

A. ASAR Image Formation Algorithm and Radiation Center Model

Before presenting the radiation center model for antenna radiation data, we shall first review the ASAR image formation algorithm presented earlier in [1] and provide some motivations for the radiation center model. To form an ASAR image from antenna radiation data, we first assume the antenna is located at the origin as shown in Fig. 3. The scattered electric field around $-x$ direction from a scattering point $P(x_o, y_o, z_o)$ on the platform can be approximated by

$$E^s(\omega,\phi,\theta) \cong A \cdot e^{-jk(r_o+x_o)} \cdot e^{-jk_o\phi y_o} \cdot e^{-jk_o\theta z_o} \tag{1}$$

where A is the strength of the scattered signal, $r_o = \sqrt{x_o^2+y_o^2+z_o^2}$ is the path traveled by the radiated signal from the antenna to point P, k is the free-space wave number, and k_o is the wave number at the center frequency. A small-angle small-bandwidth approximation is used to arrive at the above expression. By setting $u = r + x$ and utilizing the linear dependence of the phase terms in (1) on frequency and angles, we can take the 3-D inverse Fourier transform of the scattered electric field with respect to k, $k_o\phi$, and $k_o\theta$ to generate a 3-D ASAR image as follows:

$$\begin{aligned}\mathrm{ASAR}(u,y,z) &= \mathrm{IFT}_3\{E^s(\omega,\phi,\theta)\} \\ &= \mathrm{IFT}_3\{A \cdot e^{-jku_o} \cdot e^{-jk_o\phi y_o} \cdot e^{-jk_o\theta z_o}\} \\ &= A \cdot \delta(u-u_o) \cdot \delta(y-y_o) \cdot \delta(z-z_o). \end{aligned} \tag{2}$$

To convert the image into the original xyz-space from the uyz-space, we can use the transformation formula

$$x = \frac{1}{2}\left(u - \frac{(y^2+z^2)}{u}\right). \tag{3}$$

Therefore, by Fourier processing of the multifrequency multi-aspect radiation data, the point P on the platform can be mapped to a peak in the image at its correct spatial location (x_o, y_o, z_o). To summarize, the ASAR imaging process consists of 3 steps: 1) collect multifrequency multi-aspect radiation field data $E^s(\omega,\phi,\theta)$; 2) take the 3-D inverse Fourier transform to form the image in the (u,y,z) domain; and 3) use the u-to-x transformation in (3) to generate the final image in the desired (x,y,z) domain.

Although the ASAR formation methodology outlined above can be applied to general radiation data from either measurement or simulation, we have also developed an algorithm especially tailored for the SBR technique called the image-domain formulation. This derivation will serve as the basis of our radiation center model. In applying the SBR technique to the antenna radiation problem, rays are first shot from the phase center of the antenna and traced according to geometrical optics. At the exit point of each ray before they leave the platform altogether, a ray-tube integration is carried out to find the contribution of each ray to the total radiated field at various frequencies and observation angles. Therefore, the radiated field can be expressed as a weighted sum of all the rays that have been shot from the antenna

$$E^s(\omega,\phi,\theta) = \sum_{i\,\text{rays}} \alpha_i \cdot e^{-jku_i} \cdot e^{-jk_o\phi y_i} \cdot e^{-jk_o\theta z_i} \tag{4}$$

where α_i is proportional to the field strength at the exit ray-tube and is only weakly dependent on aspect and frequency. (x_i, y_i, z_i) is the location of the last hit point, and $u_i = d_i + x_i$, where d_i is the total path traveled by ith ray from the antenna to the last hit point. Since the ASAR image is generated from multifrequency multi-aspect data via Fourier inversion, we can interchange the order of the inverse Fourier transform and the ray summation and carry out the inverse Fourier transform for each ray in closed form. The resulting ASAR image is given by

$$\mathrm{ASAR}(x,y,z) = \sum_{i\,\text{rays}} \beta_i \cdot h(x-x_i, y-y_i, z-z_i) \tag{5}$$

where

$$\begin{aligned} h(x,y,z) = {} & e^{-jk_o(r+x)}\,\mathrm{sinc}\,(\Delta k x) \\ & \cdot \mathrm{sinc}(k_o\Delta\phi y) \cdot \mathrm{sinc}(k_o\Delta\theta z). \end{aligned} \tag{6}$$

The detailed derivation of this image-domain formula can be found in [1] and will not be repeated here. In the expression, (x_i, y_i, z_i) is the location of the hit point on the target for the ith ray. (For a multiple-bounce ray, it can be shown that its down range x_i is delayed by the additional travel distance from the antenna to the last hit point, while its cross range positions y_i and z_i correspond to those of the last time point.) β_i is the ray amplitude Δk, $\Delta\phi$, $\Delta\theta$ are the half-bandwidths in the k-, ϕ- and

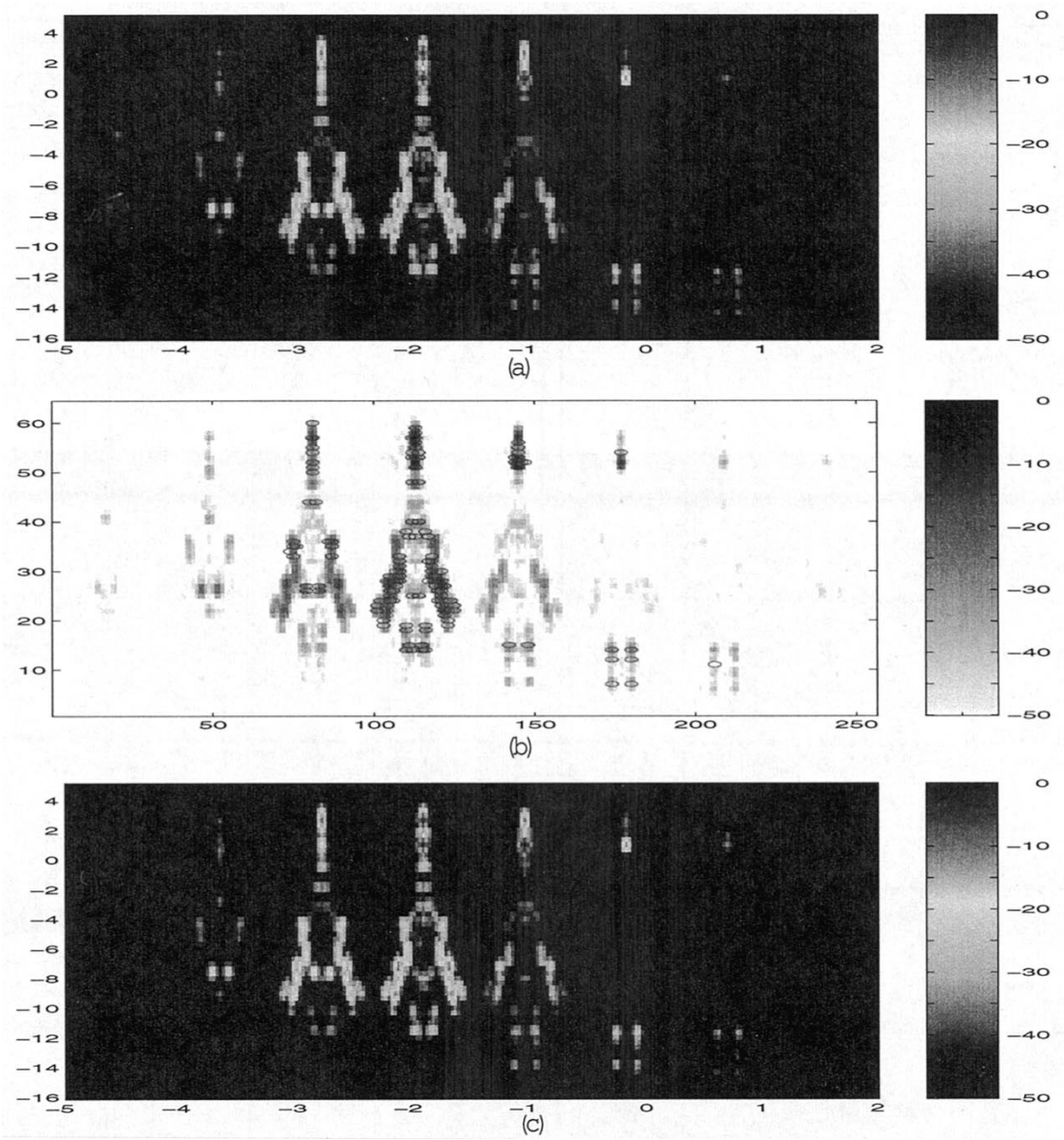

Fig. 2. (a) 3-D ASAR image of the platform generated from the simulated frequency-aspect radiation data about the nose using the code Apatch. (b) The locations of the 150 radiation centers extracted from the 3-D ASAR image using CLEAN. (c) Reconstructed 3-D ASAR image using the extracted radiation centers.

θ-domains, respectively. A key observation from (5) and (6) is that we can form the ASAR image using SBR on a ray-by-ray basis directly in the image domain. Each ray contributes to a spot centered about (x_i, y_i, z_i) in the ASAR image, with the footprint of the spot governed by the 3-D ray spread function h, which plays a role similar to the point-spread function used in the radar community. Therefore, we have shown based on SBR that the ASAR image is composed of a collection of point radiators.

Since tens of thousands of rays are traced in the SBR process, this may imply that tens of thousands of point radiators are needed to adequately represent an ASAR image. However, as we have observed from Fig. 3(a), the ASAR image of a complex platform is actually quite sparse. This is because rays interfere with one another to give rise to strong coherent scattering over only a small localized portion of the target. Therefore, an ASAR image can be accurately represented by only a limited number of radiating centers. We adopt a point radiator model which has exactly the same form as (5) to parameterize the ASAR data

$$\mathrm{ASAR}(x,y,z) \approx \sum_{\substack{n \text{ radiation} \\ \text{centers}}} A_n \cdot h(x-x_n, y-y_n, z-z_n) \tag{7}$$

where $h(x,y,z)$ is given in (6). The remaining task is to determine (x_n, y_n, z_n), the locations of the radiation centers, and A_n, their corresponding strengths.

B. Extraction and Reconstruction Algorithms

To carry out the parameterization in (7), we apply the image processing algorithm CLEAN. The CLEAN algorithm is a popular deconvolution technique in radio astronomy [10] and has been successfully utilized for scattering center extraction [6].

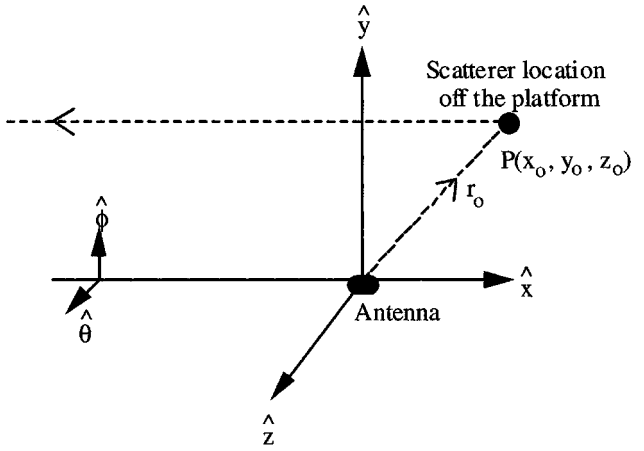

Fig. 3. Path of the radiated signal due to a scattering point P on the platform.

It is a robust iterative procedure that successively picks out the highest point in the image, assumes it is a radiating center with the corresponding strength, and removes its point spread response from the image. At the nth iteration, if A_n is the strength of the highest point in the image with locations (x_n, y_n, z_n), the 3-D residual image is found by

$$[\text{3-D Residual Image}]_{n+1} = [\text{3-D Residual Image}]_n - [A_n \cdot h(x - x_n, y - y_n, z - z_n)]. \tag{8}$$

The extraction process is iterated until the maximum in the residual image reaches a user-defined threshold. Typically, the energy in the residual image decreases quickly during the initial stages of the iteration and tapers off after reaching a noise floor.

As an example, the 3-D ASAR image in Fig. 2(a) is parameterized using the 3-D CLEAN algorithm. The ASAR image is formed using the multifrequency multi-aspect radiation data computed using Apatch for the dipole-airplane configuration shown in Fig. 1. The center frequency is 10 GHz with 0.56 GHz of bandwidth sampled over 64 frequencies. The observation angles are centered about the nose of the airplane and range between -1.67° and 1.67° in azimuth sampled over 32 points and between -0.86° and 0.86° in elevation over eight points. In the ASAR image formation, we use only the scattered field from the airplane and not the direct radiation from the antenna. Therefore, only the platform effect is imaged. Fig. 2(b) shows the locations of the extracted radiation centers from the 3-D ASAR image of Fig. 2(a) using the 3-D CLEAN algorithm. A total of 150 radiation centers are extracted from the image and their locations are plotted in Fig. 2(b) as small circles. We observe that most of them are concentrated around the $z = -2$ m cut which corresponds to the top surface of the airplane. The remainders are located on the two tails. Fig. 2(c) shows the reconstructed ASAR image from the 150 extracted radiating centers. The agreement between the original image and the reconstructed one is quite good over a dynamic range of 50 dB. Once we have extracted the radiation center model from the ASAR image, we can reconstruct the frequency and aspect radiation patterns of the antenna-platform structure. The reconstruction formula is essentially the Fourier transform of (7) and is given by

$$E^s(\omega, \phi, \theta) = \sum_n A_n \cdot e^{-jk(r_n + x_n)} \cdot e^{-jk_o \phi y_n} \cdot e^{-jk_o \theta z_n}. \tag{9}$$

By applying the above formula, we reconstruct the platform radiation patterns in frequency and aspect using the 150 radiation centers. Fig. 4(a) shows the comparison between the reconstructed frequency domain data and the original Apatch data calculated over the 0.56-GHz bandwidth about 10 GHz. The observation angle is along the nose. Fig. 4(b) shows the comparison between the reconstructed azimuth data calculated over the 3.33° window about the nose. The frequency is 10 GHz and the elevation angle is 0°. As shown from the graphs, good agreement is achieved between the reconstructed data and the original data over the frequency and aspect from which the radiation center model was generated.

III. Radiation Center Applications

In the previous section, it is shown that the radiation center model for an arbitrary antenna-platform configuration can be extracted using the ASAR-CLEAN methodology. In this section, we present two examples of the utilities of such radiation center representation.

A. Radiation Data Compression

The antenna radiation pattern on an electrically large platform is, in general, a very rapidly varying function of frequency and aspect. In this example, we shall demonstrate how the radiation center concept developed in the last section can be utilized to create a sparse model of the antenna-platform radiation over frequencies and aspect angles, thus achieving data compression. Note that for a complex platform, the radiation center model extracted at a particular observation angle is not expected to be valid over large angular extent. This is due to shadowing and other complex multiple scattering phenomena. Therefore, to fully characterize the antenna-platform radiation at all aspects, we need to extract 3-D radiation center models at various angles on a uniform grid in both elevation and azimuth. Once the radiation center models are extracted at all the angles on the grid, we can obtain the radiated field at any arbitrary angle by table lookup and reconstruction. The key question in this construct is the granularity of the grid, which, in practice, will depend on the platform complexity as well as the needed accuracy in the reconstruction. In our example, we restrict our attention to the azimuth direction, as shown in Fig. 5. The antenna-platform configuration is the same that shown in Fig. 1. First, the 3-D ASAR images for different observation angles in the azimuth direction are generated using Apatch. The angular granularity is chosen to be 5° so that a total of 72 images are generated in covering the full 360° azimuth in the zero elevation plane. Notice that only a one-time ray shoot is needed from the antenna in constructing the 72 ASAR images because of the bistatic nature of the ASAR scenario. This is contrary to the monostatic radar signature studies we have carried out previously [12]. We use a center frequency of 10 GHz and a bandwidth of 0.49 GHz. To

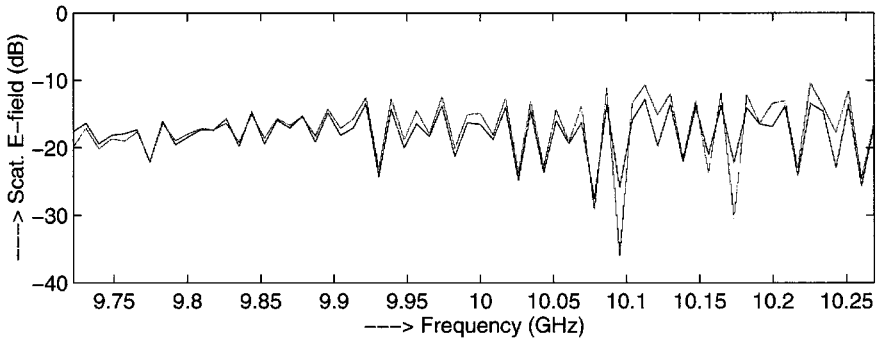

(a)

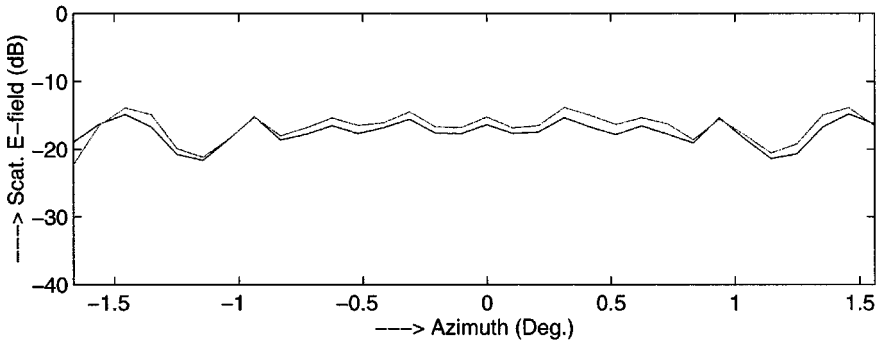

(b)

Fig. 4. Comparison of the original and the reconstructed radiation patterns. (a) Frequency sweep. (b) Azimuth sweep.

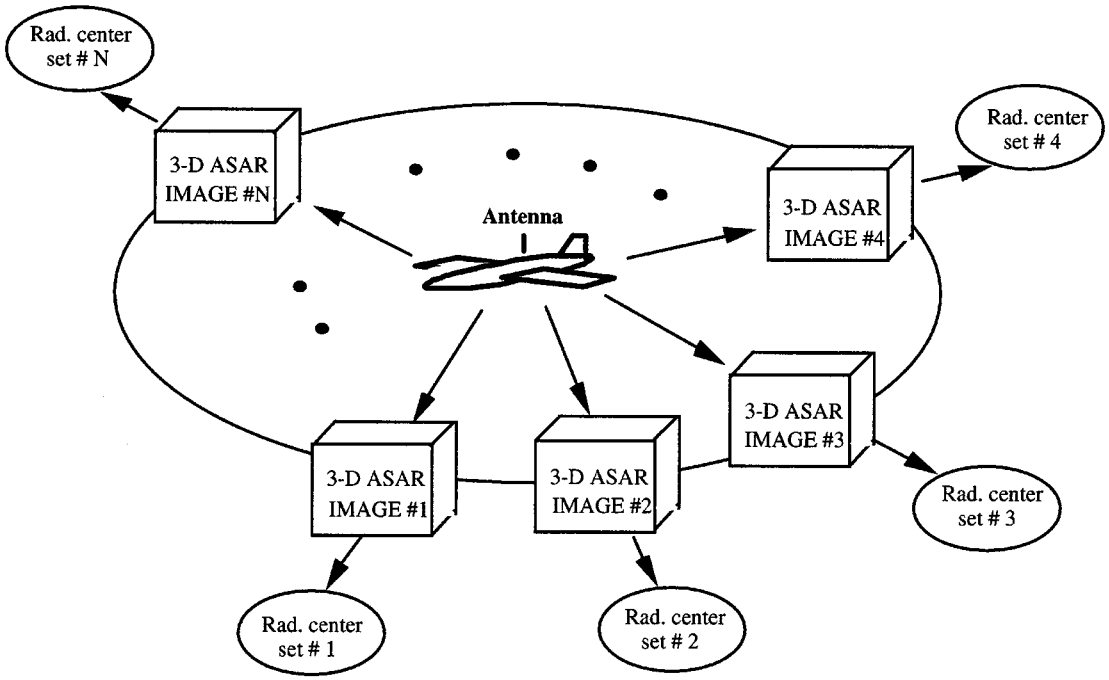

Fig. 5. Global radiation center representation of the radiation pattern along the azimuth cut obtained via ASAR image formation and radiation center extraction at various angles.

generate each ASAR image, the azimuth bandwidth is chosen to be 2.22° and the elevation bandwidth is taken as 2.46°.

Next, we extract 100 radiation centers from each of the 72 3-D ASAR images using CLEAN. Shown in Fig. 6 are four reconstructed ASAR images at 0°, 30°, 60°, and 90° with respect to the nose of the airplane. They are 2-D projected images formed by summing up all the z-slices of the original 3-D images. We observe that there are some persistent hot spots on the nose and the right wing of the airplane, which appear to be visible in all four images, while other features have smaller visibility extent. To test the validity of the model, the platform radiation pattern in the 0°–180° azimuth range is reconstructed

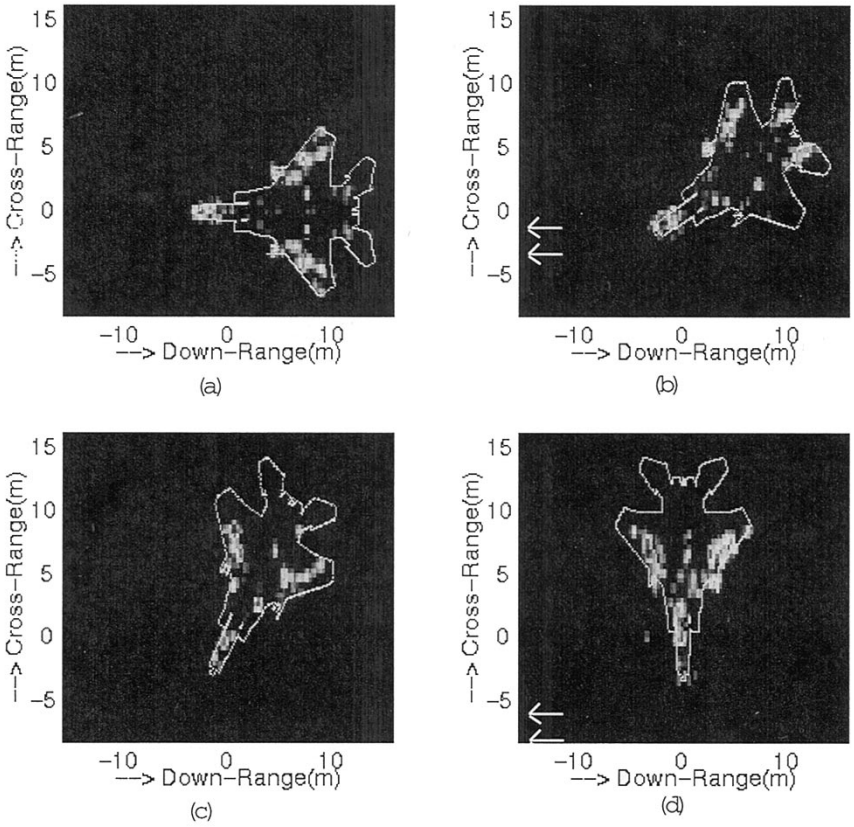

Fig. 6. 2-D projected ASAR images reconstructed from the radiation center model at different observation angles. (a) 0°. (b) 30°. (c) 60°. (d) 90°.

over each 5° sector by using the extracted radiation centers and (9). It is shown as the solid line in Fig. 7(a). Also plotted in dashed line in the figure is the original azimuth radiation pattern computed using Apatch at a granularity of 1°. Note that the reconstructed data can be computed to any desired fine angular granularity very rapidly from the radiation center model. The Apatch data, on the other hand, are computed very coarsely as it is very time-consuming to generate. The two curves show some agreement in overall trend, although the exact Apatch data are too grossly undersampled. In Fig. 7(b), the comparison between the two curves computed on the same fine granularity of 0.07° over the 30°–35° sector is shown. The reconstructed data from 30°–32.5° are reconstructed from one set of radiation centers while those from 32.5°–35° are reconstructed from another set. Note that the data between 31.11° and 33.89° correspond to "extrapolated" data based on the nearest-neighbor radiation center model. The overall agreement between the two sets of data are fairly good, even in the extrapolated region. We have also attempted to extend the extrapolation to a 10° window, and have noticed significant degradation in the outer regions of extrapolation. Therefore, the 5° granularity seems to be a good choice for this example. Reconstruction fidelity can be improved by using more radiation centers in the CLEAN procedure and by reducing the angular granularity. This, of course, is at the expense of model sparsity. Finally, the same philosophy can also be applied to the elevation direction to fully exploit the scheme for data compression. The data compression ratio achievable using the 3-D radiation center model can be roughly estimated as follows. We assume the original radiation data cover the entire visible sphere and 64 frequency samples. The original complex radiation data set, sampled at a granularity of 0.1°, requires a total storage space of $(360/0.1)*(180/0.1)*(64)*(8\text{ bytes}) = 3.3$ Gb. The radiation center model contains 100 radiation centers per angle, with each radiation center requiring the storage of five real numbers (three for the location and two for the complex amplitude). By using a 5° granularity to cover the entire visible sphere, the storage space required for the radiation center set amounts to $(360/5)*(180/5)*(100)*(5)*(4\text{ bytes}) = 5.2$ Mb. The data compression ratio is about 640 : 1. To summarize, we have shown that a global sparse radiation center model can be constructed. Once available, it can be used to reconstruct radiation data to a very fine granularity with good fidelity.

B. Platform Effect Reduction

In the second example, we shall utilize the radiation center representation to carry out a platform effect reduction study. Since the radiation centers pinpoint the locations of the dominant secondary scattering on the platform, one way to mitigate such undesirable effects is to place absorbers at those locations. This is analogous to carrying out signature reduction work using ISAR images as a guide. We use the same example as that in Section III-A and first generate the radiation center representations of the scattered field over 360° azimuth at 5° angular granularity. Next, those radiation centers that contribute more than -25 dB to the radiated field are pinpointed. To eliminate these radiation centers, we identify the facets on the target that correspond to the locations of the radiation centers and convert them from perfect conductors into perfect absorbers. By using this

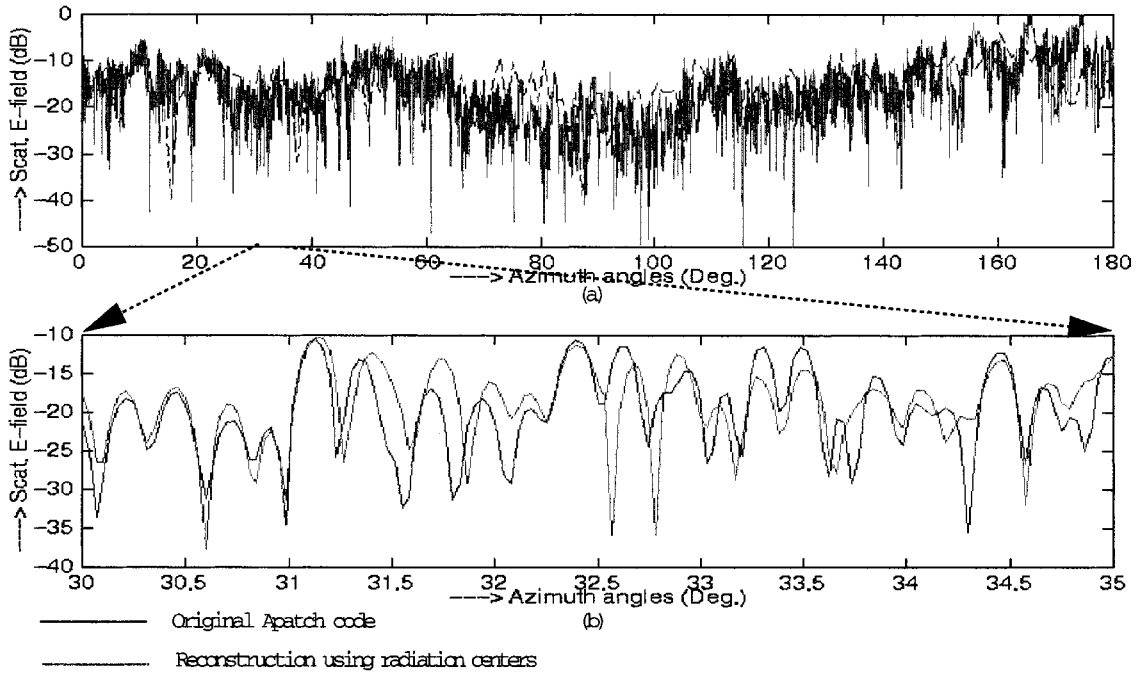

Fig. 7. Comparison of the azimuth radiation patterns from the original data and the reconstructed data based on radiation centers. (a) Coarse comparison between 0° and 180°. The original data are sampled at 1° while the reconstructed data are sampled at 0.07°. (b) Detailed comparison between 30° and 35° at the same fine angular granularity.

logic, we end up with 387 absorbing facets on the platform out of approximately 8000 facets that describe the airplane. The new CAD file is shown in Fig. 8(a), where the absorbing facets are marked in a darker shade. Fig. 9(a) shows the azimuth radiation pattern from the platform before and after the absorber coating. The patterns are computed by Apatch. We observe that the platform scattering is significantly reduced by using the absorbers. However, the resulting platform radiation level is not suppressed below the −25-dB design level as expected. In particular the platform scattering near the 20° and 170° directions remains quite high. This can be explained by the fact that the ASAR imaging algorithm is based on the single-bounce assumption. Multiple-bounce mechanisms are not correctly mapped to the platform in the ASAR image, but are rather delayed in the downrange direction [1].

To circumvent this problem and further reduce the platform scattering from multiple bounce mechanisms, we devise a scheme to tie each radiation center back to the ray mechanism that gave rise to it. The basic idea is to save the hit point information of the ray which contributes the largest amount of energy to a particular ASAR image pixel during the SBR-based image formation process in (5). Consequently, during the CLEAN procedure, each extracted radiation center has an associated "hit point list" to allow tie-back of the radiation center to the specific hit point locations on the platform. Such tie-back information is only approximate, but has been found to be very useful in radar signature and target identification applications [12]. It is important to point out that this information can be extracted only if an SBR-based approach is used to generate the ASAR image. Using this new tie-back information for each radiation center, we can now place absorbers on those facets associated with the hit points on the target. In fact, we only need

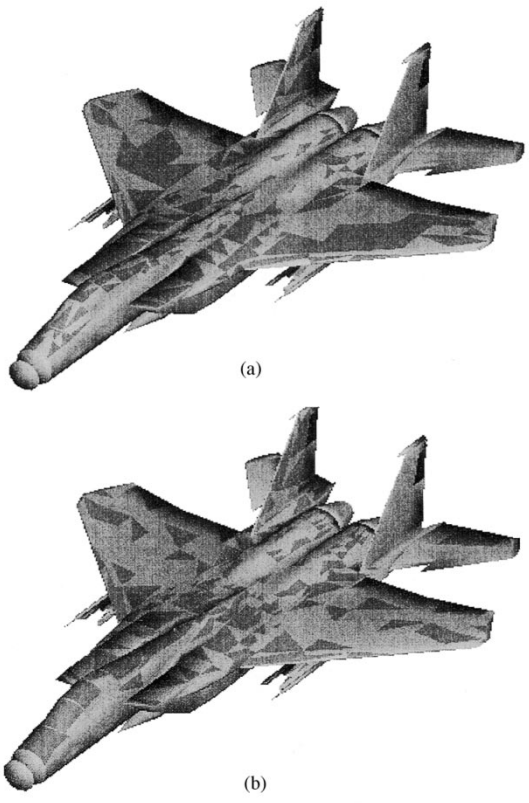

Fig. 8. CAD models with the absorbing facets shown in a darker shade. (a) Absorber placement using the first scheme in which the facet closest to a radiation center is changed into an absorber. (b) Absorber placement using the second scheme in which the hit point list for a radiation center is found via SBR and the facet from the first hit is changed into an absorber.

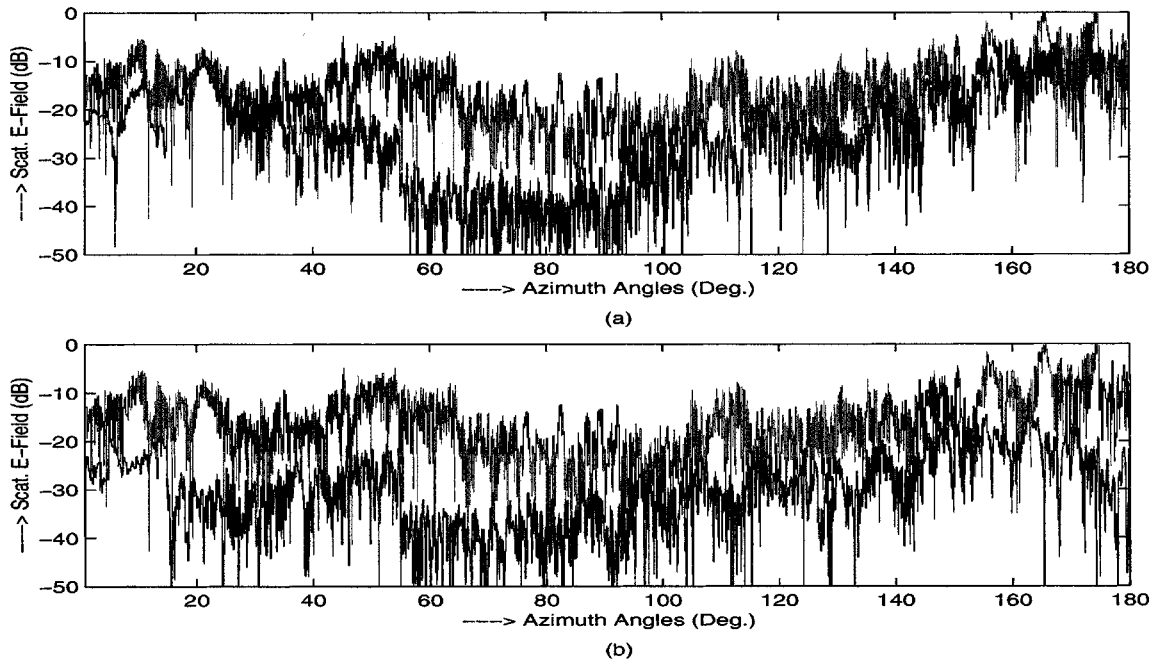

Fig. 9. Azimuth radiation patterns before and after putting absorbers on the platform. (a) Absorber placement according to the first scheme. (b) Absorber placement according to the second scheme.

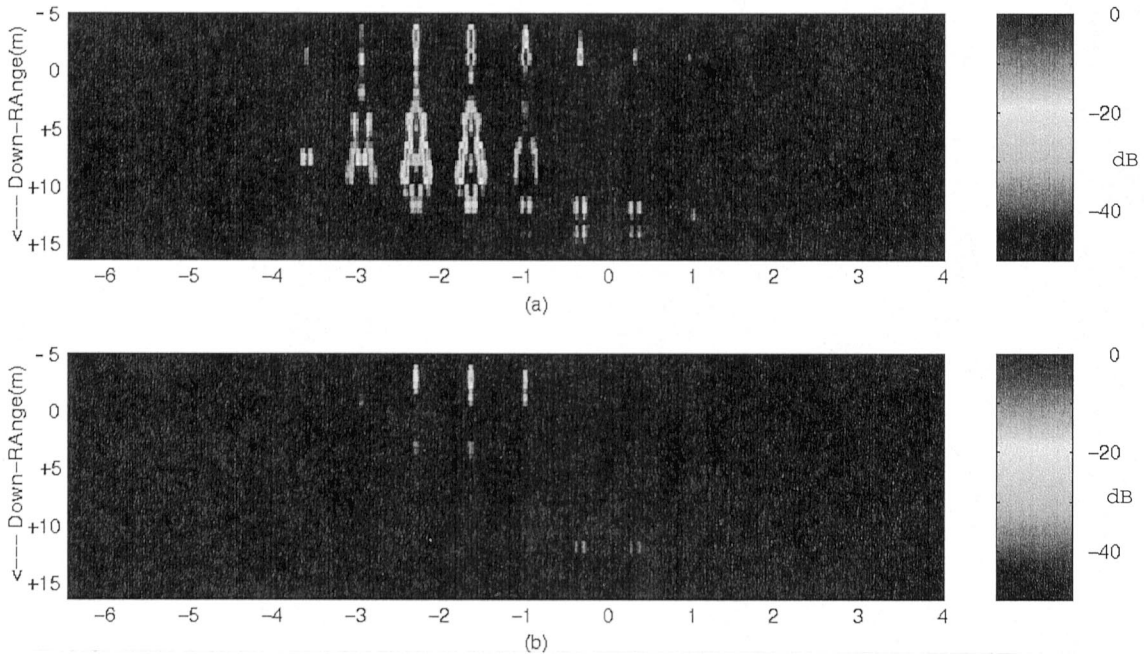

Fig. 10. 3-D ASAR images observed along the nose sector. (a) No absorbers. (b) With absorbers.

to put an absorber on any one of the hit points to eliminate the contribution. We have chosen to do so for all the first-bounce facets. A total of 403 absorbing facets on the platform are selected in this manner out of the 8000 facets. Fig. 8(b) shows the absorber-coated airplane model. Note the difference in the absorbing facet locations in Fig. 8(a) and (b). Fig. 9(b) shows the platform scattering pattern resulting from this approach. The scattering pattern of the uncoated platform is again plotted in the figure for reference. We can see that the radiation from the platform is now much better suppressed when compared to the first scheme. The scattered field from the platform comes fairly close to meeting the −25-dB design level at most of the angles. In particular the platform scattering at 20° and 170° directions is well suppressed. Fig. 10(a) and (b) shows the 3-D ASAR images of the platform scattering along the nose sector before and after the absorber treatment, respectively. We observe that the platform image nearly vanishes after the absorber coating, with the remaining stray radiation coming from the nose portion of the airplane. Note that in this example the absorber coating is placed on only one facet for each

radiation center selected, no matter how small the facet. Since a radiation center is formed by the coherent radiation from the induced current over some finite region of the platform, some minimum area may be required to more effectively eliminate the radiation from each scattering center. We believe this is the cause for the remaining stray radiation, especially near the nose and the back of the airplane, where the facets in the CAD model are very small.

In this example, we have carried out an exercise to suppress platform radiation by selectively coating the platform from the radiation center information. The first scheme is simply based on placing absorbers at the radiation center location. It works well for suppressing the single-bounce mechanisms. The second improved scheme is based on the hit point list generated during the radiation center extraction procedure. It improves performance by more effectively tracking the locations of the multibounce mechanisms. However, this scheme is more restrictive since it requires the SBR simulation algorithm be used for ASAR image formation.

IV. Conclusion

In this paper, we presented a sparse representation of antenna radiation pattern on a complex platform. This representation is based on a point radiator model that describes the radiation pattern by a collection of radiation centers on the platform. The methodology for obtaining the radiation center model is to first generate the 3-D antenna synthetic aperture radar imagery of the platform and then to parameterize the resulting image by a collection of point radiators via the CLEAN algorithm. It was shown that once such a representation is obtained, we can reconstruct and extrapolate antenna radiation patterns over frequencies and aspects with good fidelity, thus achieving high data compression ratio. Furthermore, it was shown that when coupled with the SBR simulation engine, the resulting radiation center information can be used to pinpoint cause-and-effect in platform scattering and provide important guidelines for reducing platform effects. Finally, we should point out that the data used throughout this paper were based on ray-tracing simulation. Validation from measurement or more rigorous numerical data was not attempted. However, we have since carried out the same radiation center modeling using the computational electromagnetics data from a full-wave simulator. That result is being reported in [13]. It is shown that the conclusions reached in this paper holds true even for more rigorously computed data. Measurement results of ASAR images have also been reported recently in []

References

[1] C. Ozdemir, R. Bhalla, L. C. Trintinalia, and H. Ling, "ASAR—Antenna synthetic aperture radar imaging," *IEEE Trans. Antennas Propagat.*, vol. 46, pp. 1845–1852, Dec. 1998.

[2] S. W. Lee, *User's Manual for APATCH*. Champaign, IL: DEMACO, Inc., Oct. 1992. version 1.0.

[3] H. Ling, R. Chou, and S. W. Lee, "Shooting and bouncing rays: Calculating the RCS of an arbitrary shaped cavity," *IEEE Trans. Antennas Propagat.*, vol. 37, pp. 194–205, Feb. 1989.

[4] J. Baldauf, S. W. Lee, L. Lin, S. K. Jeng, S. M. Scarborough, and C. L. Yu, "High frequency scattering from trihedral corner reflectors and other benchmark targets: SBR versus experiment," *IEEE Trans. Antennas Propagat.*, vol. 39, pp. 1345–1351, Sept. 1991.

[5] R. Bhalla and H. Ling, "A fast algorithm for signature prediction and image formation using the shooting and bouncing ray technique," *IEEE Trans. Antennas Propagat.*, vol. 43, pp. 727–731, July 1995.

[6] ——, "Three-dimensional scattering center extraction using the shooting and bouncing ray technique," *IEEE Trans. Antennas Propagat.*, vol. 44, pp. 1445–1453, Nov. 1996.

[7] W. P. Yu, L. G. To, and K. Oii, "N-point scatterer model RCS/glint reconstruction from high-resolution ISAR target imaging," in *Proc. End Game Measurement and Modeling Conference*, Point Mugu, CA, Jan. 1991, pp. 197–212.

[8] N. Y. Tseng and W. D. Burnside, "A very efficient RCS data compression and reconstruction technique," ElectroSci. Lab., Ohio State Univ., Columbus, OH, Tech. Rep. 722 780-4, Nov. 1992.

[9] S. Y. Wang and S. K. Jeng, "Generation of point scatterer models using PTD/SBR technique," in *IEEE Antennas Propagat. Symp. Dig.*, Newport Beach, CA, June 1995, pp. 1914–1917.

[10] A. Selalovitz and B. D. Frieden, "A 'CLEAN'-type deconvolution algorithm," *Astronom. Astrophys.*, vol. 70, pp. 335–343, 1978.

[11] J. Tsao and B. D. Steinberg, "Reduction of sidelobe and speckle artifacts in microwave imaging: The CLEAN technique," *IEEE Trans. Antennas Propagat.*, vol. 36, pp. 543–556, Apr. 1988.

[12] R. Bhalla, J. Moore, and H. Ling, "A global scattering center representation of complex targets using the shooting and bouncing ray technique," *IEEE Trans. Antennas Propagat.*, vol. 45, pp. 1850–1856, Dec. 1997.

[13] T. Su, C. Ozdemir, and H. Ling, "On extracting the radiation center representation of antenna radiation patterns on a complex platform," *Microwave Opt. Tech. Lett.*, vol. 26, pp. 4–7, July 2000.

[14] T.-H. Chu and C.-J. Pan, "Microwave diversity imaging using ASAR approach," *IEEE Antennas Propagat. Symp. Dig.*, pp. 1952–1955, July 2000.

Caner Ozdemir (S'95–M'97) was born in Edremit, Turkey, on March 29, 1971. He received the B.S. degree in electrical and electronics engineering in 1992, from the Middle-East Technical University (METU), Ankara, Turkey, and the M.S. and Ph.D. degrees in electrical and computer engineering from the University of Texas at Austin, in 1995 and 1998, respectively.

From 1992 to 1993, he worked as a Project Engineer at the electronic warfare office of the Turkish Military Electronics Industries (ASELSAN), Ankara, Turkey. From 1998 to 2000 he was a Research Scientist at Advanced Systems Technology Group (ASTG), Honeywell, Inc., Columbia, MD. Currently, he is a Faculty Member at the Electrical and Electronics Engineering Department, Mersin University, Mersin, Turkey. His primary research interests are radar signal processing and imaging, electromagnetic scattering, antenna design techniques, and computational electromagnetic.

Rajan Bhalla, photograph and biography not available at time of publication.

Hao Ling (S'83–M'86–SM'92–F'99), photograph and biography not available at time of publication.